

Constraining the size of the narrow line region in distant quasars

Atsunori Yonehara ^{1 2}

*Theoretical Astrophysics Group, Department of Physics, The University of Tokyo, Hongo
7-3-1, Bunkyo-ku, Tokyo, 113-0033, Japan*

yonehara@utap.phys.s.u-tokyo.ac.jp

ABSTRACT

We propose a proper method to measure the size of the narrow line region (NLR) in distant quasars. The apparent angular size of the NLR is, in general, too small to resolve technically. However, it is possible to map the NLR if with gravitational lensing. In our method, we directly compare the observed image of the NLR with the expected lensed images of the NLR for various source sizes and lens models. Seeking the best fit image via the comparison procedures, we can obtain the best-fit size and the best-fit lens model. We apply this method to the two-dimensional spectroscopic data of a famous lensed quasar, Q2237+0305. If the lens galaxy resembles the applied lens model, an upper limit to the NLR size can be set 750 pc. Further, we examine how the fitting results will be improved by future observations, taking into account the realistic observational effects, such as seeing. Future observations will provide us more stringent constraints on the size of the NLR and on the density profile of the lens galaxy.

Subject headings: galaxies: quasars: emission lines, galaxies: structure, gravitational lensing

1. Introduction

It is widely believed that Seyfert galaxies and quasars have a rather complex structure in their nuclei. The central engine seems to be a combination of a supermassive black hole and an accretion disk, which are surrounded by the broad-line regions (BLRs), dusty tori,

¹Inoue Fellow

²Currently, the author affiliates to ARI/ZAH (Heidelberg, Germany) by JSPS Postdoctoral Fellowships for Research Abroad. E-mail address is yonehara@ari.uni-heidelberg.de .

and the narrow line regions (NLRs) (e.g., Antonucci 1993). Therefore, investigating the nature of the NLR is useful to obtain good insight into the physics of the central engine and its environments. So far, various kinds of observational programs have been carried out to understand the basic physical processes involved with the gas in the NLRs, such as photoionization, shock excitation, and kinematics. Schmitt et al. (2003), for example, performed narrow band imaging observations of near-by Seyfert galaxies by using spatially extended [O III] λ 5007 emission line and measured the size of the NLRs. They found a correlation between the size (R_{NLR}) and the luminosity ($L_{[\text{O III}]}$) of the NLRs as $R_{\text{NLR}} \propto L_{[\text{O III}]}^{0.33 \pm 0.04}$, which significantly differs from that of quasars (Bennert et al. 2002); $R_{\text{NLR}} \propto L_{[\text{O III}]}^{0.52 \pm 0.06}$. On the other hand, Netzer et al. (2004) performed slit spectroscopy of distant quasars, and claimed the existence of two distinct populations for luminous active galactic nuclei; that is, quasars with and without the NLR. We here note, however, that such arguments are purely based on the empirical relation between R_{NLR} and $L_{[\text{O III}]}$ obtained from a relatively small number of samples (Bennert et al. 2002). It is not yet clear if this relation can be accurately extrapolated to luminous active galactic nuclei and/or high-redshift quasars. Therefore, direct measurements of the size of the NLRs in luminous and/or high-redshift quasars are necessary to confirm their findings and to explore the underlying physics. However, it is not easy to make direct measurements for distance sources, since the more distant the quasars are, the smaller the apparent size of the NLRs becomes. To make matters worse, it is hard to measure the size from narrow band imaging observations, because the wavelength of the emission line is redshifted and move out from the passband of existing narrow band filters.

We, here, consider an alternative method which utilizes the gravitational lensing, since the gravitational lensing can spatially stretch the source image. In principle, the size of the NLRs in multiple quasars can be measured more precisely, compared with that of the unlensed quasars with the same intrinsic luminosity. Thus, there have already been such attempts by using a two-dimensional spectrograph attached to a ground based telescope (Adam et al. 1989).

Mediavilla et al. (1998) performed two-dimensional spectroscopic observations of a lensed quasar with quadruple image, Q2237+0305 (or Huchra’s lens), by using an optical fiber spectrograph, INTEGRAL. They focused on an arc-like feature in the image of not [O III] λ 5007 but C III] λ 1909 emission line and derived the size of the NLR in Q2237+0305 to be $\sim 400h^{-1}$ pc. Motta, Mediavilla, Munoz, Falco (2004) used the same observational data, but decomposed the spectra into two components; the broad line component and the narrow line component. They then made two maps for the two spectral components, finding a significant difference between them in terms of the spatial extent of the line emitting regions. After making two images, they focused on the arc-like feature again and derive a size of the NLR to be 700 \sim 900 pc. This value is consistent with that obtained by Mediavilla et

al. (1998). Wayth, O’Dowd, Webster (2005), in contrast, could not find an arc-like feature in the data taken by the GMOS Integral Field Unit (IFU), claiming that the size of the NLRs is significantly smaller than that obtained by Mediavilla et al. (1998). They remove the seeing effects via the deconvolution technique, but did not decompose the spectra into the narrow line and the broad line component. Since their analysis are different not only in the used data but also in the adopted analysis procedures, we cannot simply compare their results nor conclude which is more appropriate. Importantly, the lens model degeneracy, which was pointed out by Wambsganss, Paczyński (1994), was not properly considered in these works.

In this paper, we consider a more reliable method to measure the size of the NLRs in lensed quasars, taking into account the effect of seeing and the lens model degeneracy in a proper way and then apply our method to both real data and simulated data. In the next section, we explain our method to measure the size of the NLRs. The results obtained by the currently available data is presented in section 3. In section 4, we examine a potentiality of our method for future observational data. The final section is devoted for concluding remarks. A concordance cosmology with $\Omega_m = 0.3$, $\Omega_\Lambda = 0.7$, and $H_0 = 70 \text{ km s}^{-1} \text{ Mpc}^{-1}$ (or $h = 0.7$) is used throughout this paper.

2. Our Method

2.1. Procedures

For a given emissivity profile of the source and for a given lens model, we can calculate an ideal image of the extended lensed source (see next subsection for the lens model). Convolution of the ideal image with a point spread function which represents the seeing effect, we can obtain an expected image for the observation with an infinite spatial resolution. Re-sampling this expected image with a finite spatial resolution, which is same as the spatial sampling rate of an observational instrument, we can produce an image expected by the given observational instrument. By calculating such images for various source sizes and various lens models, and comparing them with the observed one, we can finally obtain the best-fit source size and the best-fit lens model.

Here, we apply χ^2 - minimization method to find the best-fit solution. The total χ^2 - is calculated as,

$$\chi^2 = \sum_{i=1}^{N_{\text{obs}}} \frac{(f_{\text{obs},i} - f_{\text{model},i})^2}{\sigma_i^2}, \quad (1)$$

where N_{obs} , $f_{\text{obs},i}$, $f_{\text{model},i}$, and σ_i are the number of data points, the observed flux of the i -th data point, the i -th predicted flux from a given model, and the observational error of

the i -th data point, respectively.

Unless otherwise specified, we assume that the source is circularly symmetric and that the emissivity profile of the source (ϵ) is expressed by Gaussian;

$$\epsilon(r) \propto \exp\left(-\frac{r^2}{R_{\text{NLR}}^2}\right), \quad (2)$$

where r represents the distance from the source center.

Further, we assume that the point spread function due to the seeing effect is also circularly symmetric and has a Gaussian profile with the same “full width half maximum” as that of the seeing size.

2.2. Lens model

It is too hard to measure the size of the NLR without any constraint on the lens model, we put a practical assumption on the model that the mass density profile of the lens galaxy is elliptical and is expressed by a power-law in radial profile. Since there exists the so-called lens model degeneracy (e.g., Wambsganss, Paczyński 1994) even in such situation, we need lens models with various density profiles to find reliable constraints on the size of the NLR. For simplicity, we adopt so-called “generalized pseudo-isothermal elliptic potential” or “tilted Plummer family of elliptic potential” (Blandford, Kochanek 1987). In this model, the lens potential (ϕ) at an image position of $\vec{\theta} = (\theta_x, \theta_y)$ is given by

$$\phi(\vec{\theta}) = \alpha_{\text{E}}^{2-2\lambda} [\theta_c^2 + (1-e)\theta_x^2 + (1+e)\theta_y^2]^\lambda, \quad (3)$$

where α_{E} , e , λ and θ_c represents the lens size, the ellipticity, the power index and the core radius of the lens potential, respectively. There are other models that represent ellipticity of the lens galaxies, such as softened power-law elliptical mass distribution model (Barkana 1998), or other similar lens models with power-law density profile (Schramm 1990; Keeton 2001). Even more sophisticated lens models that consist from bulge, disk, and halo component can be used in this kind of studies. It is also interesting to perform the same study by using different type of lens models, but main purpose of the current study is to investigate how the method works. Moreover, such models require relatively much computational expense, and in a current paper, we only focus on a lens model which represented by equation 3. Dependence on different type of lens models will be discussed in a future paper.

A model with large (small) λ corresponds to a shallow (steep) density profile. In particular, the density profile with $\lambda = 0.5$ is identical to that of the singular isothermal sphere

model. Since the fifth image has not been detected yet (Falco et al. 1996), we set $\theta_c = 0$ which is equivalent with the lack of the fifth image for this model. As was claimed by Kassiola, Kovner (1993), $e > \frac{\lambda}{3-\lambda}$ should be satisfied in this model, since otherwise the iso-density contour shows concave shape and such model must be unrealistic for a single lens object.

For various λ , we try to reproduce the positions of the quadruple image of Q2237+0305 relative to the position of the lens galaxy ¹. The number of observable is $2 \times 4 = 8$, i.e., x - and y - coordinate of the four images. Since observed fluxes may be affected by microlensing and/or differential dust extinction, we do not take into account the flux ratios between the four images in our fitting procedure. The number of free parameters is 6 that is, α_E , e , λ , x - and y - coordinate of the source, and the direction of the major axis of the lens model. Thus, degree of freedom in this fitting procedure is $8 - 6 = 2$. χ^2 values of the best-fit lens model for various λ are presented in the bottom panel of figure 1. The resultant values of α_E and e which obtained by this fitting procedure is also presented in the middle and the top panel of figure 1, respectively. Within $3\text{-}\sigma$ confidence level, a wide range of λ , $\lambda = 0.41 \sim 0.77$, is acceptable for the model to reproduce the observed image positions. Even if we restrict $1\text{-}\sigma$ confidence level, the model with $\lambda = 0.44 \sim 0.73$ provides an acceptable fit, and the acceptable range does not shrink so much. This represents the lens model degeneracy as was found through the previous studies.

From this fitting procedures, we obtain the best-fit parameters of the lens model for a given λ as shown in the middle and the top panel of figure 1. Hereafter, we treat the density profile (or λ) as a single free parameter for the lens model in our proposed method; once we change λ value, other parameters such as e are automatically replaced with the best-fit parameters for new λ value. We put a constraint on e value to keep a condition that is claimed by Kassiola, Kovner (1993) during the fitting procedures, i.e., $e \leq \frac{\lambda}{3-\lambda}$. We can see the effect of this constraint in the top panel of figure 1. Basically, the best fit value of α_E and e becomes larger, when the applied λ value for the fitting procedure becomes smaller. Though the best fit value of α_E gradually increases with decreasing λ until the smallest value of λ for the fitting ($\lambda = 0.4$), that of e faces the limiting value of the constraint on the fitting, i.e., $e = \frac{\lambda}{3-\lambda}$, at $\lambda \sim 0.46$. Below this λ value, the best fit value of e is almost identical to the limiting value of e . Therefore, we would like to mention that the validity of the fitting results at this small λ regime is somewhat uncertain.

Finally, R_{NLR} and λ is the parameter to be determined from our method. Calculated ideal images, which are to be compared with the observed image of Q2237+0305, are shown in figure 2. In the case of large R_{NLR} and/or large λ , the expected image tends to exhibit

¹The data are taken from CASTLES website, <http://cfa-www.harvard.edu/castles/>.

an arc- or ring-like morphology, as is clearly seen in figure 2. Even if we consider the seeing effect, obviously, we can recognize differences between the images for the different parameter sets. Therefore, we can, in principle, constraint the size of the NLRs and the lens model via our proposed method.

3. Analyses using the Current Data

Motta, Mediavilla, Munoz, Falco (2004) have performed Gaussian fit to the emission line profiles in observed spectra, and have decomposed the detected emission line into a broad line component and a narrow line component. The resultant line intensity peak (I) and line width (w) of both components of the C III] λ 1909 emission line are shown in table 1 of Motta, Mediavilla, Munoz, Falco (2004). Since total flux of an emission line with Gaussian profile is calculate by $\sqrt{\pi}Iw$, we evaluate the total flux ($\sqrt{\pi}Iw$) of both emission line components at each fiber from the quantities, I and w , presented in table 1 of Motta, Mediavilla, Munoz, Falco (2004). Error of flux at each fiber is estimated by using the error of the line intensity peak(δI) and that of the line width (δw) as usual manner; the error is equal to $\sqrt{\pi}\sqrt{I^2 \cdot \delta w^2 + w^2 \cdot \delta I^2}$. Consequently, we can estimate the goodness of fit, i.e., the χ^2 value, between a model and the observational data via equation 1. This procedure could be applicable if the emission line was detected, and if the decomposition into the broad line component and the narrow line component was succeeded. However, the emission line was not detected in some fibers, e.g., fiber 107 of Motta, Mediavilla, Munoz, Falco (2004). In such case, the total observed flux is set to be zero and the error is set to be the same as the error of a fiber that the total flux is the weakest in emission line detected fibers. The χ^2 value of such fibers can also be estimated via equation 1. Additionally, even if an emission line is detected, decomposition into the broad line component and the narrow line component might not be succeeded in some fibers, e.g., fiber 105 of Motta, Mediavilla, Munoz, Falco (2004). In such case, the emission line is treated as a single component in table 1 of Motta, Mediavilla, Munoz, Falco (2004), and the total observed flux is set to be an upper limit for both components and the error for both components is evaluated from the same observational data. If a model flux of a fiber exceeds the observed flux of the fiber, the χ^2 value of the fiber is evaluated by equation 1. If a model flux of a fiber is below the observed flux of the fiber, the χ^2 value of the fiber is set to be zero.

The spatial sampling rate is set to be the same as INTEGRAL, and it is roughly 0.5 arcsec in the case of Motta, Mediavilla, Munoz, Falco (2004). Both of the shape of a fiber cross section and the flux loss between fibers were taken into account. As reported in Motta, Mediavilla, Munoz, Falco (2004), seeing is set to be 0.7 arcsec. We make use of

the data of $6 \times 6 = 36$ fibers, in total, in a rectangular array. Since the number of the fitting parameter is two; R_{NLR} (or R_{BLR} for BLR) and λ , degree of freedom in the fitting is $36 - 2 = 34$. The following results are summarized in the upper part of table 1.

3.1. Broad line region

The Gaussian intensity peak for the broad line component is presented in table 1 of Motta, Mediavilla, Munoz, Falco (2004), but the Gaussian width for the broad line component is not. Thus, following the analysis by Motta, Mediavilla, Munoz, Falco (2004), we set the width to be $71 \pm 11 \text{ \AA}$ for all fiber. The searched parameter ranges of R_{BLR} and λ are $50 \sim 2050 \text{ pc}$ and $0.4 \sim 0.8$, respectively. The best fit parameter search is performed with 50 pc resolution in R_{BLR} and 0.01 resolution in λ . The result is presented in figure 3a. The best fit parameters are $R_{\text{BLR}} = 50 \text{ pc}$ and $\lambda = 0.47$ ($\chi^2 = 28.01$). However, even if we allow $1\text{-}\sigma$ confidence level, a wide range of λ values are acceptable and R_{BLR} cannot be constrained tightly. To get more reliable result, we had better to choose $3\text{-}\sigma$ confidence region, rather than $1\text{-}\sigma$ confidence region. Unfortunately, in such case, most of the parameter set is acceptable as seen in figure 3a, and we can say nothing about the lens model and the size of the BLR. Consequently, we cannot put any useful constraint on density profile of the lens model from the available data. We can only put an upper limit to the size of the BLR as $R_{\text{BLR}} < 400 \text{ pc}$ in $1\text{-}\sigma$ confidence level.

3.2. Narrow line region

We use the same technique to investigate NLRs. The Gaussian intensity peak for the narrow line component and the Gaussian width for the narrow line component are taken from table 1 of Motta, Mediavilla, Munoz, Falco (2004). The searched parameter ranges and the resolution are the same as those in the case for the BLR. The fitting result is presented in figure 3b. Again, the best fit parameter is $R_{\text{NLR}} = 50 \text{ pc}$ and $\lambda = 0.47$ ($\chi^2 = 25.09$), but wider ranges of R_{NLR} and λ are acceptable. However, there are two major differences between figure 3a and b. Firstly, the upper limit on R_{NLR} is significantly larger than that on R_{BLR} in $1\text{-}\sigma$ confidence level. Secondly, the parameter ranges in the upper right part of figure 3b must be rejected, even if we allow $3\text{-}\sigma$ confidence level. Unlike Motta, Mediavilla, Munoz, Falco (2004), we are not able to measure R_{NLR} from the data. Its upper limit is $\sim 750 \text{ pc}$ in $1\text{-}\sigma$ confidence level. Again, we are not able to put useful constraints on the lens model as in the case of the BLRs.

4. Analyses by using Improved Data

From the fitting results presented in the previous section, we understand that the currently available data is not good enough to measure the size of the NLR and to constrain on the lens model. One reason for this can be attributed to the large spatial sampling rate in the used data, but this can easily be improved. Rather, better smaller spatial sampling rates with the same signal-to-noise (hereafter, S/N) ratio have already been achieved technically (Wayth, O’Dowd, Webster 2005). For instance, actually, GMOS-IFU on the Gemini North, SINFONI on VLT, or KYOTO-3DII on SUBARU telescope (Sugai et al. 2004) can provide us with two-dimensional spectra with 0.1 arcsec spatial sampling rate. Thus, it is worth of testing the potentiality of the proposed method for the data with 0.1 arcsec spatial sampling rate. In this section, we make mock observational data, which have better sampling rate, for a given parameter set (λ and R_{NLR} or R_{BLR}), and apply our method to those data to see how nicely it can reproduce the given parameter values.

4.1. Our procedures

Throughout this section, we adopt $R_{\text{NLR}} = 1000$ pc and $\lambda = 0.5$. In this lens model, the best fit value of α_{E} and e is 0.887 arcsec and 0.138, respectively. Then, we can calculate the expected observational images for a given spatial sampling rate, which is currently set to be 0.1 arcsec. Moreover, observational noise is artificially added to the expected image, and we obtain mock observational data. There may be several sources of noise, but we assume so-called photon noise to be dominant. Unless otherwise specified, seeing size is fixed to be 0.7 arcsec² and the noise at the peak flux is set to be 10 %. Data from $41 \times 41 = 1681$ fibers are used for fitting. Roughly 4 arcsec \times 4 arcsec field is covered, which is sufficient for our purpose. Since the number of parameters are 2 (R_{NLR} and λ), degree of freedom for the fitting is $1681 - 2 = 1679$. The following results are summarized in the lower part of table 1.

4.2. Seeing effects

The result is shown in figure 4a. The best fit parameter is $R_{\text{NLR}} = 1000$ pc and $\lambda = 0.5$ ($\chi^2 = 1637.47$). In 1- σ confidence level, the acceptable range of the parameters are still large, and the lens model degeneracy still remains in part. Even so, however, we can put tighter constraints on the parameters than for the currently available data (see figure 3). The

²This value is somewhat worse compared with typical seeing at Mauna Kea site.

acceptable ranges in $1\text{-}\sigma$ confidence level are $R_{\text{NLR}} \simeq 600 \sim 1300\text{pc}$ and $\lambda \simeq 0.45 \sim 0.59$. Therefore, we can nicely reproduce the given parameters with $\sim 40\%$ accuracy for R_{NLR} and $\sim 18\%$ accuracy for λ .

The result in the case of smaller seeing size is shown in figure 4b. Again, the best fit parameter is $R_{\text{NLR}} = 1000 \text{ pc}$ and $\lambda = 0.5$ ($\chi^2 = 1634.92$). Areas of all of the three confidence regions are smaller than those in the previous case (see figure 4a), although the differences are small. The acceptable ranges in $1\text{-}\sigma$ confidence level are $R_{\text{NLR}} \simeq 650 \sim 1300\text{pc}$ ($\sim 35\%$ accuracy) and $\lambda \simeq 0.45 \sim 0.58$ ($\sim 16\%$ accuracy). Although certain observations with better seeing will provide us with somewhat better information, the result do not alter much, compared with cases of the data with the same S/N ratio but with worse seeing.

In contrast, if the incorrect seeing size is used in the analysis, the situation will become worse. The best-fit size is expected to be smaller (larger) than true value when we overestimate (underestimate) the seeing size. For instance, if we assume 0.6 arcsec (0.8 arcsec) seeing and perform fitting to the mock observational data with 0.7 arcsec seeing, the minimum χ^2 value will exceed $3\text{-}\sigma$ level, and the best-fit size and λ will be 1500 pc (550 pc) and 0.46 (0.58), respectively. Thus, it must be crucial to know the seeing effect correctly for the success of our proposed method. The best-fit values are shifted along the sequence of degeneracy which has already been appeared in figure 4a. Since 0.1 arcsec corresponds to 850 pc at the redshift of this quasar, the difference between the true size and the best-fit size, $\sim 500 \text{ pc}$, is somewhat smaller than the difference between the assumed seeing size and the true seeing size. This may be due to the most essential effect of gravitational lensing, image stretching of the observed images, in part.

4.3. Observational errors

Next, we examine the effects of observational errors on the results by decreasing noise, or increasing S/N ratio, at the peak flux to 5%. In order to reduce observational errors to this value, roughly $(0.1/0.05)^2 = 4$ times longer exposure time is needed than that in the previous case. The result is shown in figure 4c. Again, the best fit parameter is $R_{\text{NLR}} = 1000 \text{ pc}$ and $\lambda = 0.5$ ($\chi^2 = 1648.09$), but each the confidence region becomes narrower dramatically. The acceptable parameter range in $1\text{-}\sigma$ confidence level is $R_{\text{NLR}} \simeq 850 \sim 1150\text{pc}$ ($\sim 15\%$ accuracy) and $\lambda \simeq 0.48 \sim 0.53$ ($\sim 6\%$ accuracy). Even in $3\text{-}\sigma$ confidence level for this high S/N ratio case that is shown in figure 4c, the acceptable parameter ranges are somewhat smaller than those in $1\text{-}\sigma$ confidence level for lower S/N ratio case that is shown in figure 4a.

4.4. Clumpy nature of the narrow line region

In above studies, we assumed Gaussian emissivity profile for the NLRs as given by equation 2. In actual Seyfert galaxies, however, the emissivity profile may not be smooth but can be very complex; likely to be composed of small numerous clumps. Here, we assume that the NLRs are composed of 100 clumps, the emissivity profile of each clump obeys Gaussian profile (equation 2) with a size of $R = 50$ pc. We assume that the clumps are randomly distributed and the distribution of distance between the source center and each clump obeys Gaussian distribution with the typical size of 1000 pc.

The results are shown in figure 4d. We find that the best fit values of the parameters are $R_{\text{NLR}} = 1000$ pc and $\lambda = 0.49$ ($\chi^2 = 1660.11$). The best fit value of λ is slightly smaller than the given value, but that of R_{NLR} is identical to the given value. The shape of 1- σ confidence region is different from that in figure 4a, but the overall properties, such as the direction of the major axis of 1- σ confidence region, are similar to each other. Although the extent of 1- σ confidence region in this figure is smaller than that in figure 4a, the given values are included in 1- σ confidence region, $R_{\text{NLR}} = 650 \sim 1200$ pc and $\lambda = 0.45 \sim 0.56$.

Therefore, we can safely conclude that we can put a reliable constraint on the size of the NLRs and the lens model by the proposed method, even if the clumpy nature of the NLRs are taken into account. The clumpy nature may work as an origin of the systematic error in the proposed method.

5. Concluding Remarks

In this paper, we present the potentially useful method to constrain the size of the NLR and the lens model. Taking the case of Q2237+0305 as an example, we re-analyze the two dimensional spectroscopic data taken by Mediavilla et al. (1998) and obtain reliable constraints on the size of the BLR and the NLR. Although both of the sizes are consistent with point-like source, the possibility of the extended source is still remains. The obtained upper limit to the sizes of the BLR and the NLR are 400 pc and 750 pc, respectively. As far as the mass profile of the lens galaxy is nicely represented by a model where the lens potential is elliptical and a power-law in radial profile, as we assumed in this paper, these values can be appropriate upper limits.

In addition, we have demonstrated that the currently available instruments can provide a better opportunity to explore the NLRs and the lens model. Seeing is an important factor in ground-based observations. However, it may not seriously affect our results, if we know the seeing effect correctly. Observations with higher S/N ratios and with higher spatial

sampling rates will be useful to give better constraints on the parameters. Even if the spatial distribution of the NLR is not smooth but clumpy, we will be able to reproduce the values of the basic parameters successfully.

One thing that we have to mention is so-called “mass sheet degeneracy” in gravitational lensing phenomena; if there is a mass sheet with the surface mass density of κ_s between observer and the source, any observed structure will be scaled up by a factor of $(1 - \kappa_s)^{-1}$ in length and by a factor of $(1 - \kappa_s)^{-2}$ in area. Consequently, the actual source size should be the produce of $(1 - \kappa)$ and the obtained source size ³. Though the measurement of κ_s is practically hard and annoying issue, such difficulty may be solved at least in part by observational studies of the environments around lens systems (e.g., Faure et al. 2004).

If the emissivity profile of the NLR has an elliptical shape or a double-cone shape, the lensed image of the NLR can be different from those considered in this paper and these different properties will alter the results to some extent. Further, the existence of substructures in or around the lens galaxy may also affect the observed image of the NLR (e.g., Metcalf, Moustakas, Bunker, Parry 2004). To evaluate such effects, quantitative estimations are necessary. Even in such case, however, we can, in principle, find correct values of the parameters in a statistical fashion, e.g., by searching the deepest valley of χ^2 (see figure 4), and to obtain an observational insight into the shape of the NLR and/or substructures as well as the size of the NLR and the lens model.

The author acknowledges to S. Mineshige, H. Sugai, T. Nagao, K. Yahata, W.-H. Bian, and anonymous referee for their valuable comments and discussions.

REFERENCES

- Adam, G., et al. 1989, A&A, 208, L15
- Antonucci, R.R.J. 1993, ARA&A, 31, 473
- Barkana, R. 1998, ApJ, 502, 531
- Bennert, N., et al. 2002, ApJ, 574, 105
- Blandford, R.D., and Kochanek C.S. 1987, ApJ, 321, 658

³The resultant density profile does not change due to this degeneracy, but the lens size term in equation 3, $\alpha_E^{2-2\lambda}$, should be multiplied by $(1 - \kappa_s)$ to obtain the actual value.

- Falco, E.E., et al. 1996, *AJ*, 112, 897
- Faure, C., et al. 2004, *A&A*. 428, 741
- Kassiola, A., and Kovner, I. 1993, *ApJ*, 417, 450
- Keeton, C.R., astro-ph/0102341
- Mediavilla, E., et al. 1998, *ApJ*, 503, 27
- Metcalf, R.B., Moustakas, L.A., Bunker, A.J., and Parry, I.R. 2004, *ApJ*, 607, 43
- Motta, V., Mediavilla, E., Munoz, J.A., and Falco, E. 2004, *ApJ*, 613, 86
- Netzer, H., et al. 2004, *ApJ*, 614, 558
- Schramm, T. 1990, *A&A*, 231, 19
- Schmitt, H.R., et al. 2003, *ApJ*, 597, 768
- Sugai, H., et al. 2004, *SPIE*, 5492, 651
- Wayth, R.B., O’Dowd, M., and Webster, R.L. 2005, *MNRAS*, 359, 561
- Wambsganss, J., and Paczyński, B. 1994, *AJ*, 108, 1156

Table 1. Summary of the fitting results

data	size ^a	(1- σ range)	λ	(1- σ range)	figure
BLR ^b	50	(50 ~ 400)	0.47	(0.42 ~ 0.71)	figure 3a
NLR ^b	50	(50 ~ 750)	0.47	(0.42 ~ 0.79)	figure 3b
standard ^c	1000	(600 ~ 1300)	0.50	(0.45 ~ 0.59)	figure 4a
better seeing ^c	1000	(650 ~ 1300)	0.50	(0.45 ~ 0.58)	figure 4b
smaller errors ^c	1000	(850 ~ 1150)	0.50	(0.48 ~ 0.53)	figure 4c
clumpy nature ^c	1000	(650 ~ 1200)	0.49	(0.45 ~ 0.56)	figure 4d

^a R_{BLR} for the BLR, and R_{NLR} for the NLR (unit: pc).

^bReal observational data obtained by Motta, Mediavilla, Munoz, Falco (2004) (see section 3).

^cMock observational data calculated in this paper (see section 4).

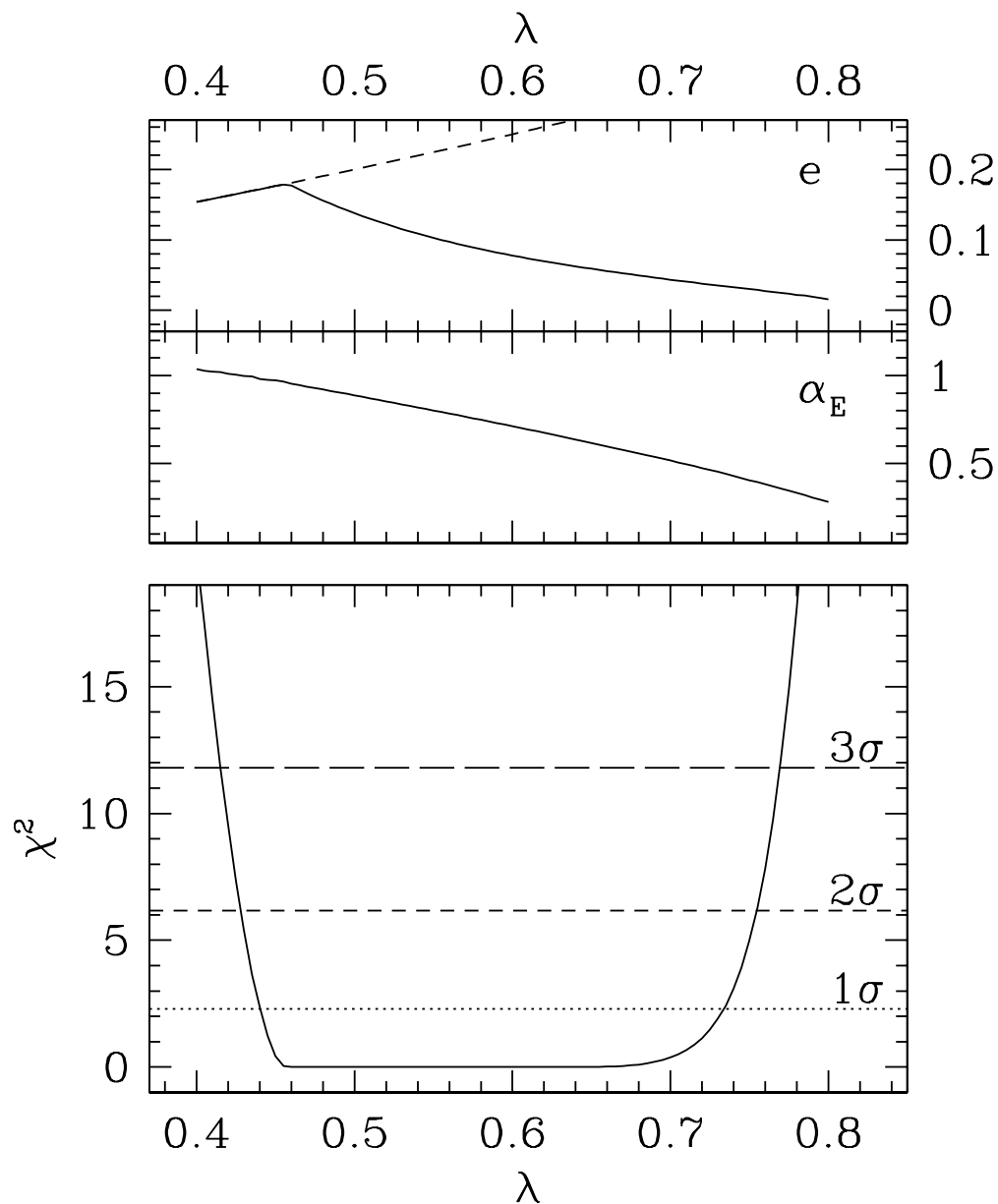


Fig. 1.— Total χ^2 value (the bottom panel), the best fit value of α_E in the unit of arcsec (the middle panel), and that of e (the top panel) is presented with solid line as a function λ . In the bottom panel, 1-, 2-, and 3- σ confidence level is also presented by the dotted, dashed, and long-dashed line, respectively. In the top panel, a critical value of e which is noted by Kassiola, Kovner (1993) (see section 2.2) is also presented with the dashed line.

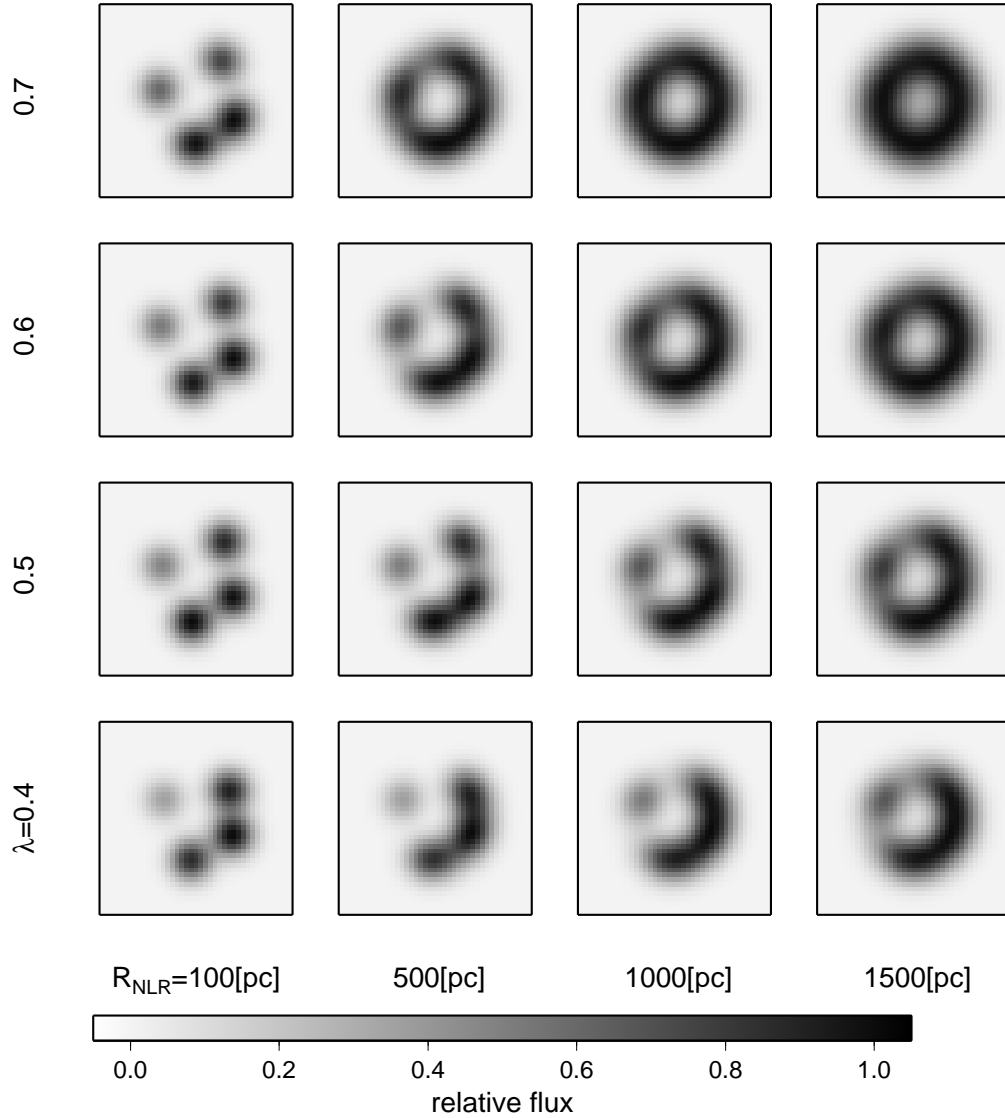


Fig. 2.— Calculated images that are to be compared with observational data. We indicate the values of R_{NLR} and λ in the bottom and in the left of the panels, respectively. The flux of each pixel is normalized by the peak flux. We assume 0.7 arcsec seeing and 0.1 arcsec sampling rate.

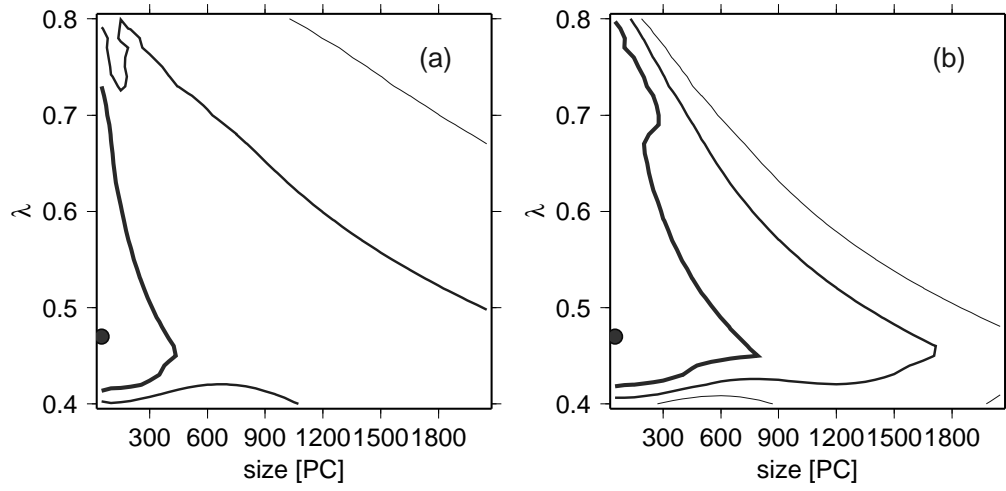


Fig. 3.— The results of fitting to the broad line component (a: left panel) and the narrow line component (b: right panel), respectively. The thick, middle, and thin lines present 1-, 2-, and 3- σ confidence levels, respectively. The filled circle indicates the best fit parameter.

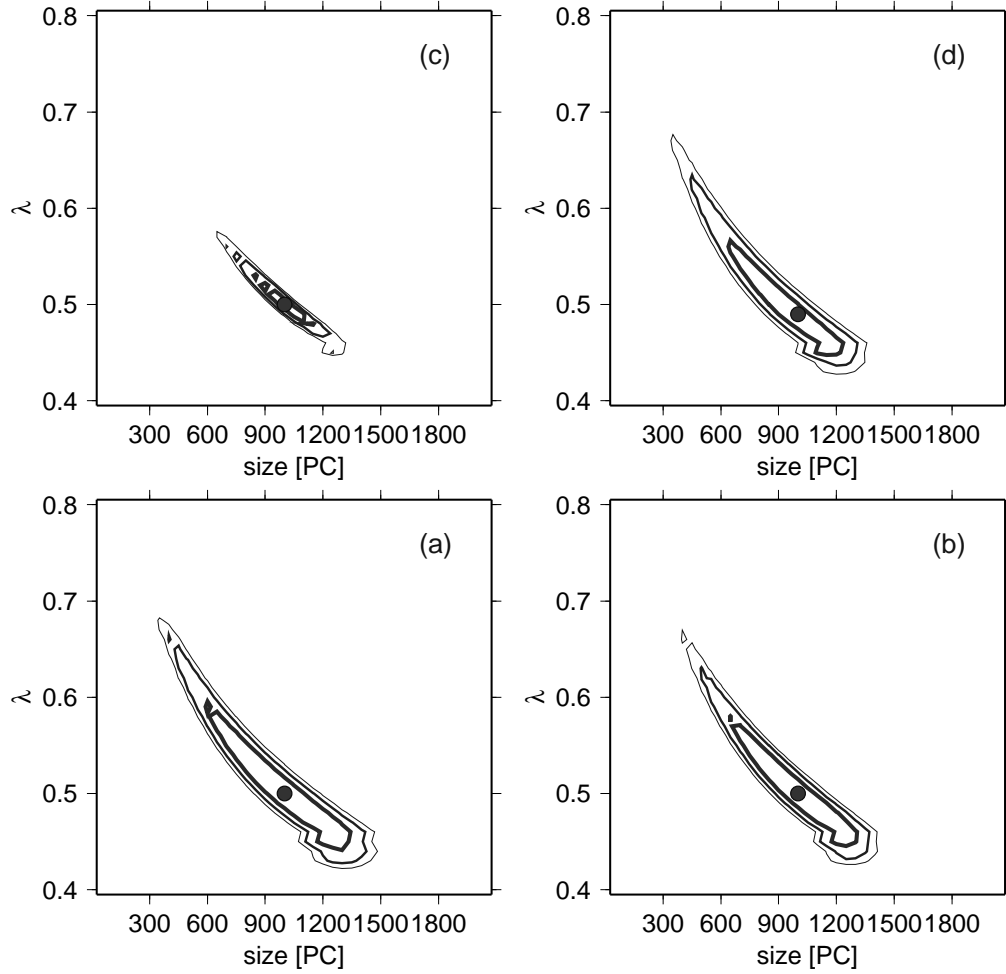


Fig. 4.— Same as figure 3, but for the mock observational data (see section 4). Panel (b) and (c) shows the result for better seeing case and smaller error case compared with panel (a), respectively. Panel (d) shows the result for the clumpy NLR.